Electronic Supplementary Material (ESI) for Nanoscale.

Supporting Information: Interfacial water and ion distribution determine ζ potential and binding affinity of nanoparticles to biomolecules

Dongyue Liang,[†,‡,⊥] Udaya Dahal,[‡,⊥] Yongqian (Kelly) Zhang,[†] Christian Lochbaum,[†] Dhiman Ray,[¶] Robert J. Hamers,[†] Joel A. Pedersen,[§,†] and Qiang Cui[*,‡,‖]

†*Department of Chemistry, University of Wisconsin-Madison, 1101 University Avenue, Madison, WI 53706*

‡*Department of Chemistry, Boston University, 590 Commonwealth Avenue Boston, MA 02215*

¶*Department of Chemistry, University of California, Irvine, 1102 Natural Sciences 2, Irvine, CA 92617*

§*Departments of Soil Science, Civil & Environmental Engineering, and Chemistry, University of Wisconsin-Madison, 1525 Observatory Drive, Madison, WI 53706*

‖*Departments of Physics and Biomedical Engineering, Boston University, 590 Commonwealth Avenue Boston, MA 02215*

⊥*Contributed equally to this work*

E-mail: qiangcui@bu.edu,Tel:(+1)-617-353-6189

1 Additional Simulation Data: Equilibrium Simulations

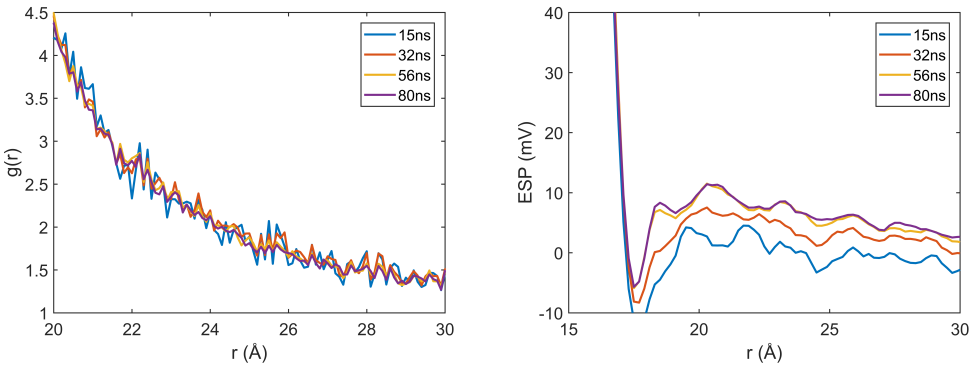

(a) (b)

Figure S1: Convergence test of Chloride radial distribution function (RDF) and Electrostatic Potential profile using C4P32-C4N33 with 150 mM NaCl as the example; both are measured relative to the center of the nanoparticle. The different curves show time-averaged profiles over different time intervals and for RDF we focus on the tail region, which is used for identifying the location of slipping plane (see main text and Fig. S5. The figures indicate that while ion distributions converge reasonably quickly within $\sim$15 ns, simulation of $\geq$80 ns is required to converge the interfacial electrostatic potential.

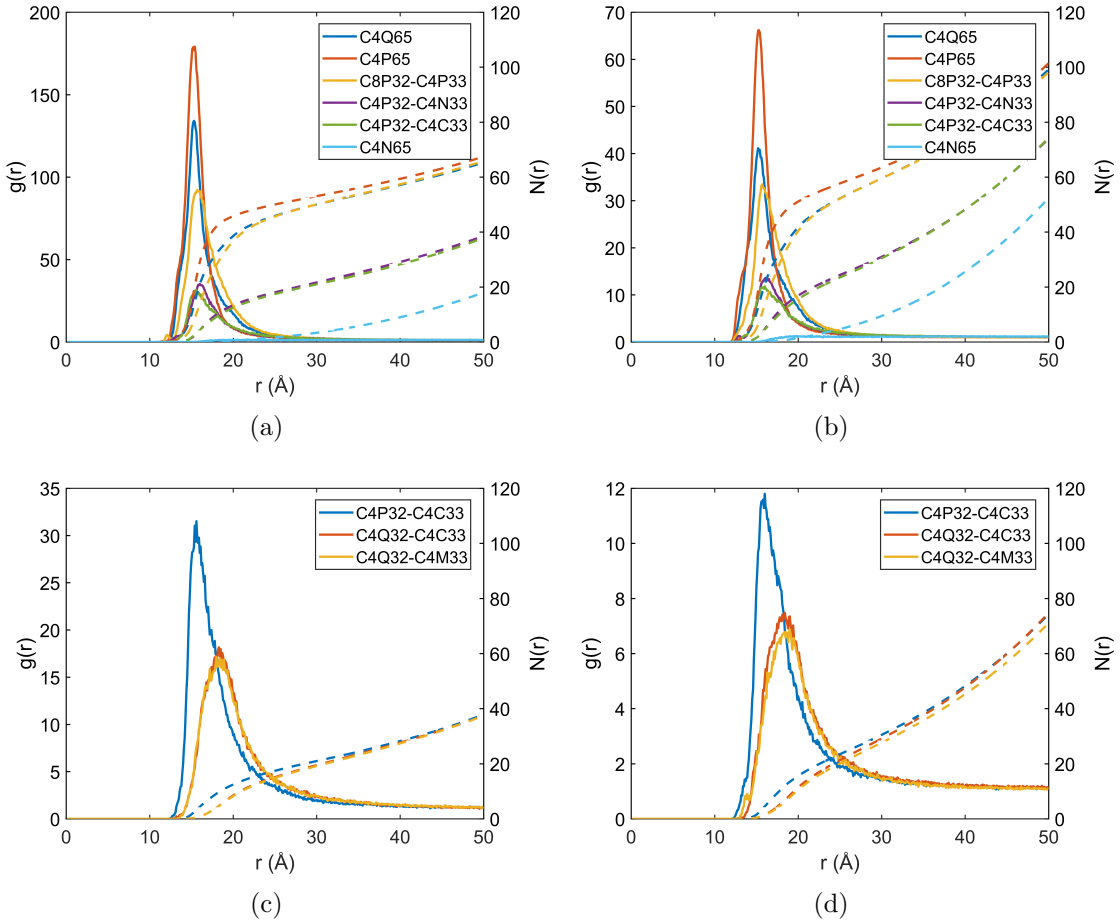

Figure S2: Radial distribution function of chloride ions with respect to the nanoparticle center; the dashed lines are integrated radial distribution functions. The left column is for 50 mM NaCl solution, and the right column is for 150 mM NaCl solution.

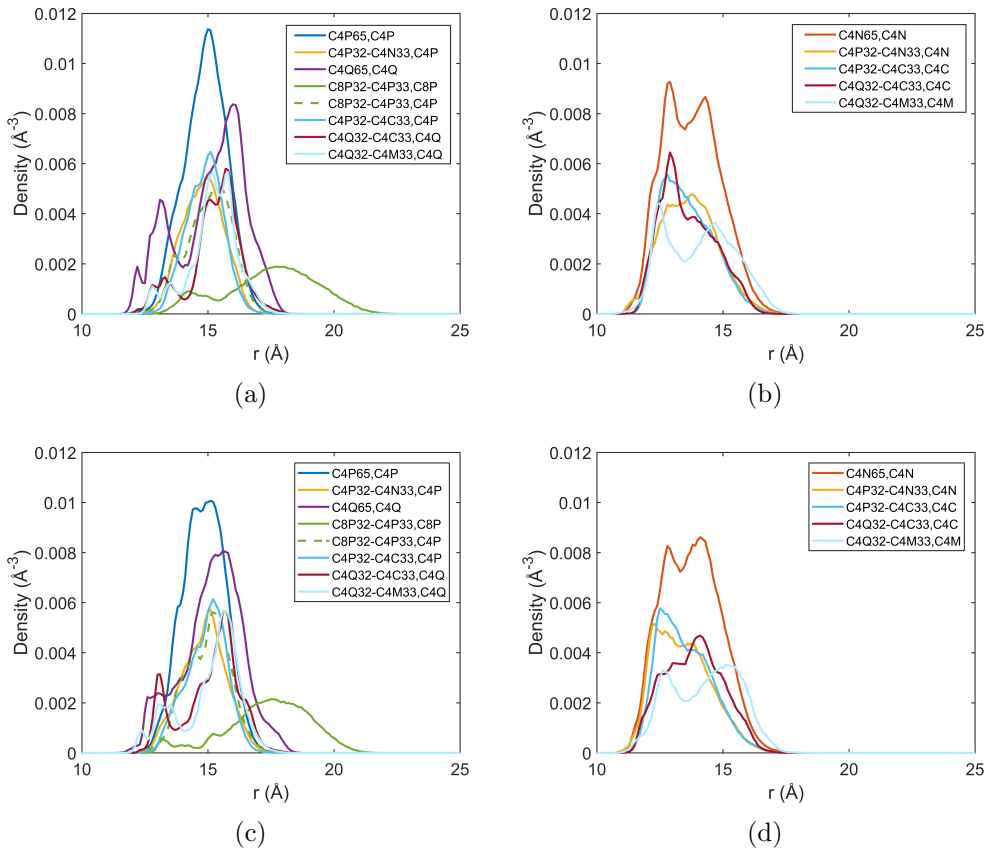

Figure S3: Number density of heavy atoms (nitrogen, carbon) in ligand head-group as a function of radial distance to nanoparticle center from equilibrium simulations with NaCl concentrations of (a-b) 50 mM and (c-d) 150 mM. The charged and neutral beads are shown in separate panels.

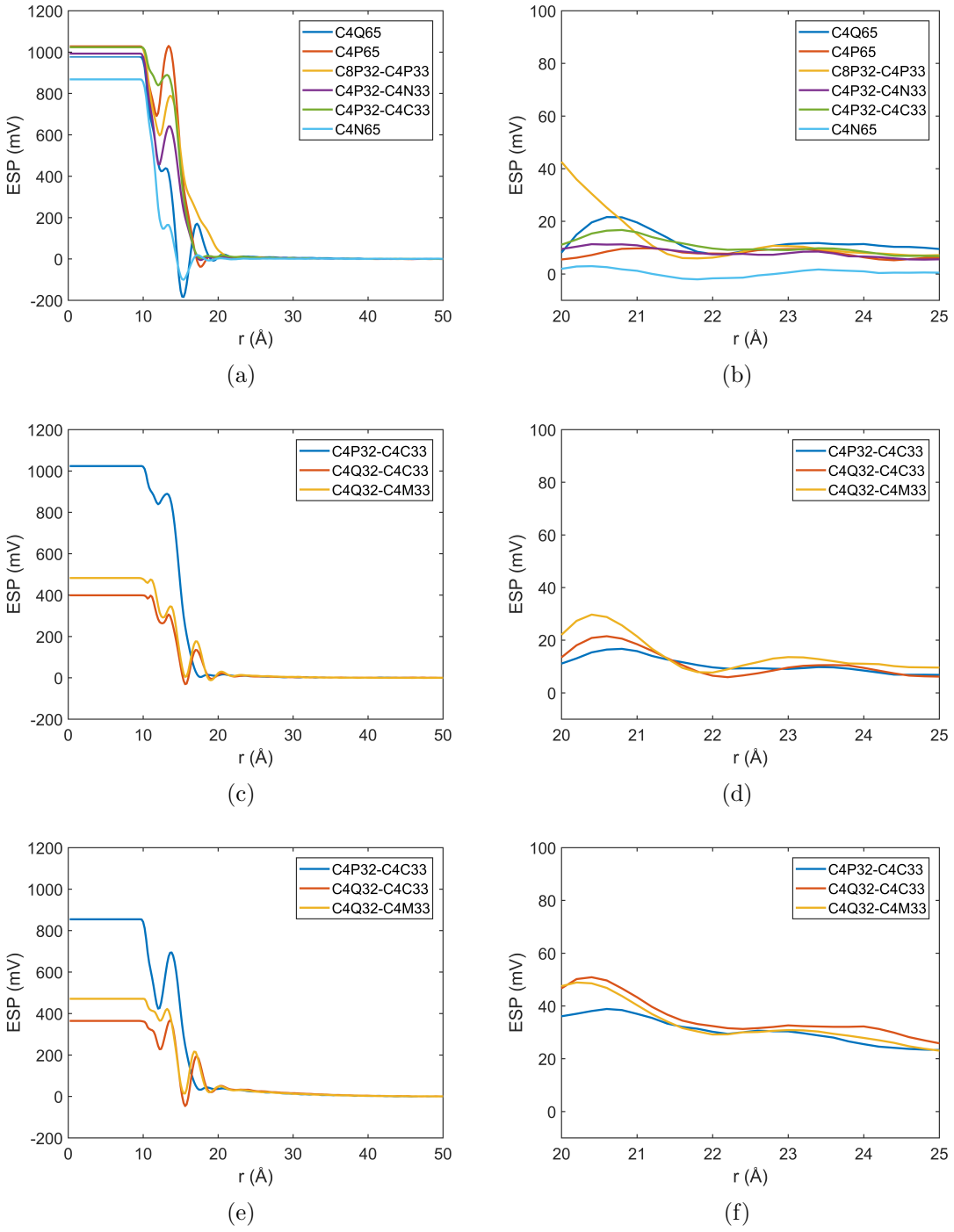

Figure S4: Additional results for the computed electrostatic potential (ESP) as a function of distance from the nanoparticle center. The left column shows the overall profile, while the right column enlarges the interfacial region. Panels (a-d) are results for 150 mM NaCl solution, (e-f) are for 50 mM NaCl solution; see Fig. 3 in the main text for the results for other particles in 50 mM NaCl solution.

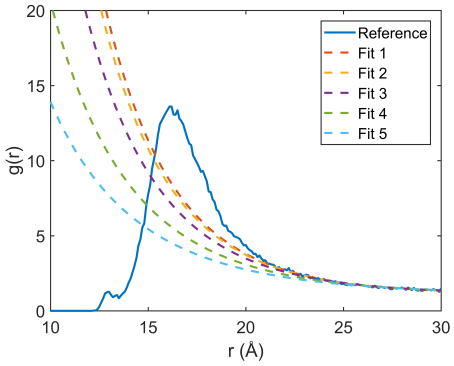

(a)

Figure S5: Use of multiple fits of chloride radial distribution function (RDF) to identify the location of the slipping plane, r_{slip}, and its uncertainty; the case shown here corresponds to C4P32-C4N33 in 150 mM NaCl solution. The tail region of the RDF is fitted to the Debye-Hückel result in the form of $A^{-Br}/r + C$, while r_{slip} is identified as the distance where the fit starts to deviate from the computed RDF. Multiple fits including data that contain different ranges of r between 21 and 30 Å are done to estimate the uncertainty of r_{slip}.

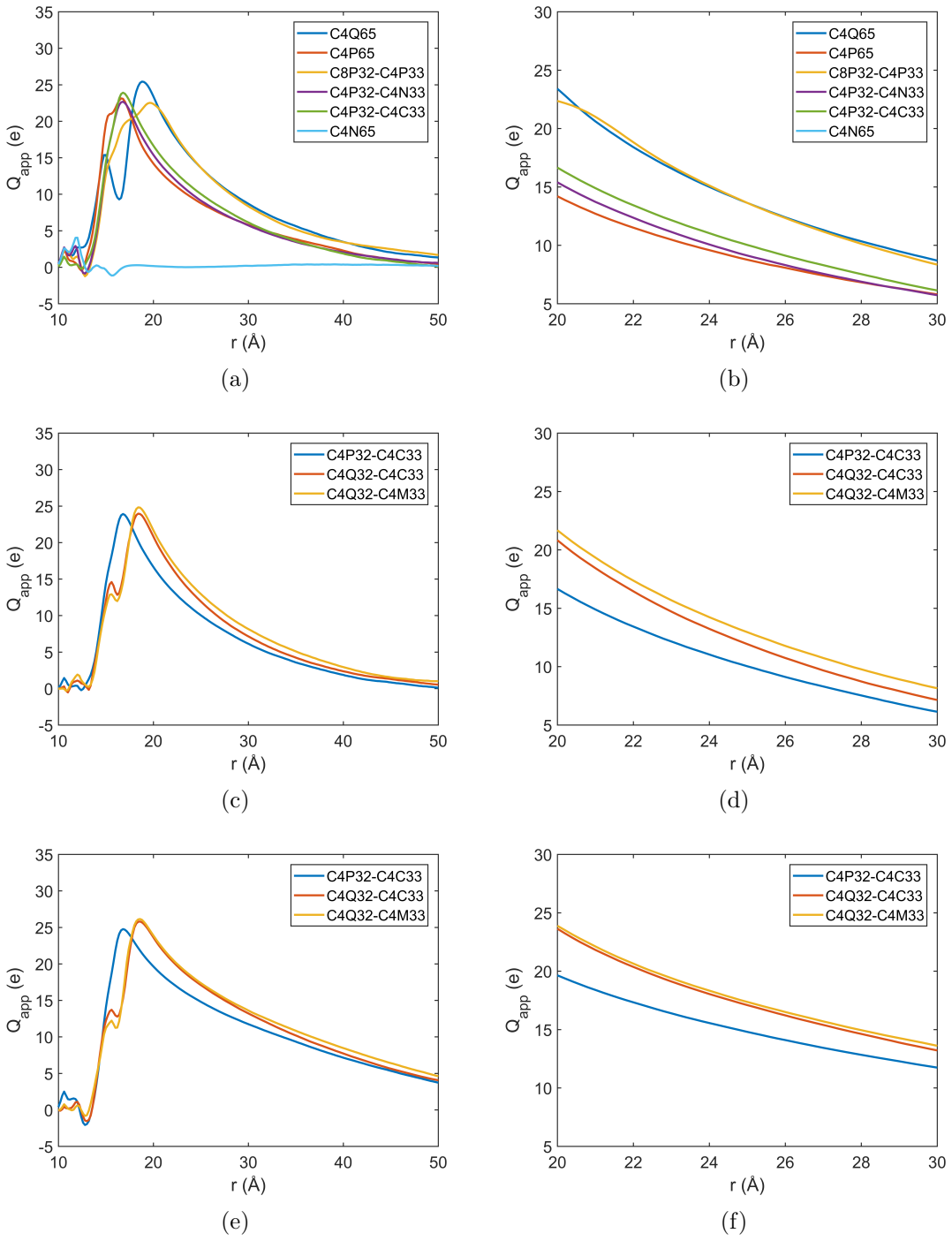

Figure S6: Additional results for the computed apparent charge ($Q_{app}(r)$) profiles as functions of distance from the nanoparticle center; $Q_{app}(r)$ includes bare ligand charges and counterion charges up to distance r. The left column shows the overall profile, while the right column enlarges the interfacial region. Panels (a-d) are results for 150 mM NaCl solution, (e-f) are for 50 mM NaCl solution; see Fig. 5 in the main text for the results for other particles in 50 mM NaCl solution.

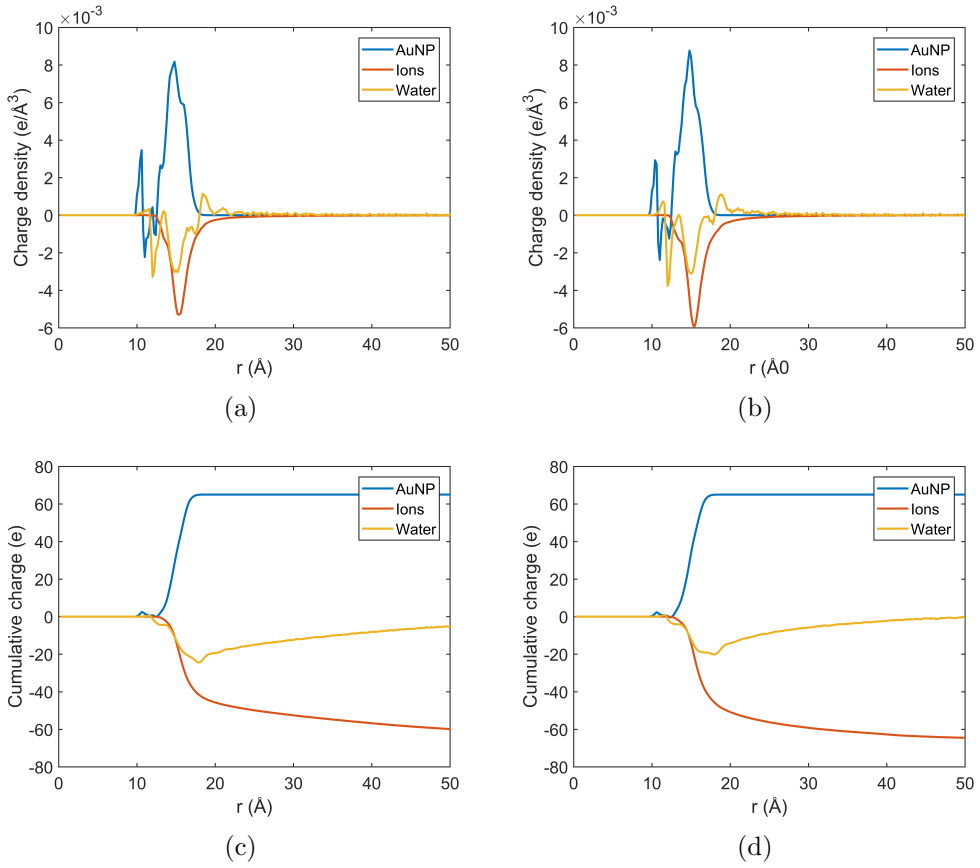

Figure S7: Contributions from different components to the interfacial charge distribution as functions of distance from the nanoparticle (C4P65) center. (a-b) plot the charge densities; (c-d) plot the cumulative charge components. The left column is for 50 mM NaCl, and the right column for 150 mM NaCl. Note that oriented water molecules make considerable contributions to the interfacial charge.

2 Additional Simulation Data: Non-Equilibrium Simulations

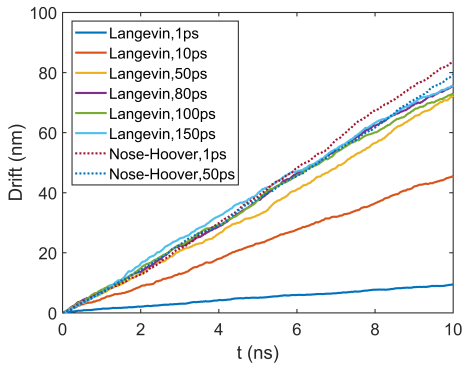

(a)

Figure S8: Drift of a C4P32 gold nanoparticle from non-equilibrium molecular dynamics simulations that employ a Langevin Dynamics (LD) or Nose-Hoover thermostat with different damping coefficients. The results show that the drift with LD is comparable with the Nose-Hoover result only when the damping coefficient is smaller than $(50\ \text{ns})^{-1}$. The electric field applied here is 0.1 kcal $\cdot$ mol^{-1} $\cdot$ Å^{-1} $\cdot$ e^{-1}. Also see Table S1 for the dependence of water diffusion on the damping coefficient.

Table S1: Diffusion coefficients (in the unit of 10^{-5} cm^2/s) of water in the simulations presented in Figure S8 with different damping coefficients in Langevin dynamics or Nose-Hoover thermostat.

Thermostat	D_{H_2O}
Langevin, 1ps	4.80
Langevin, 10ps	5.91
Langevin, 50ps	6.38
Langevin, 80ps	6.43
Langevin, 100ps	6.41
Nose-Hoover, 1ps	6.00
Nose-Hoover, 50ps	6.57

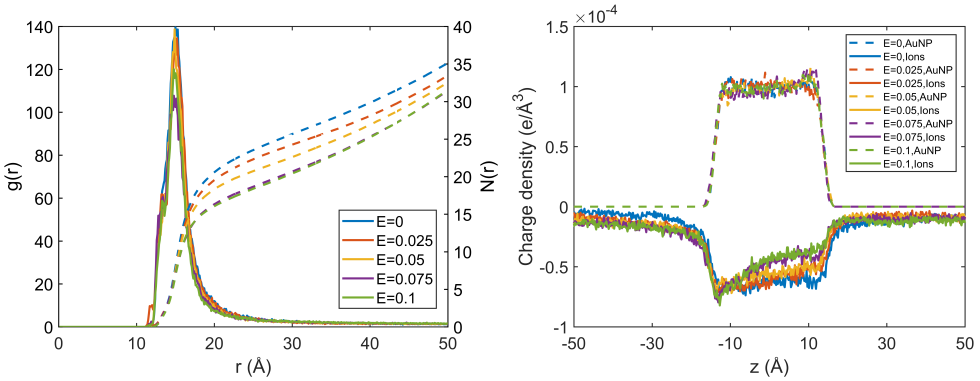

(a) (b)

Figure S9: (a) Radial distribution functions of Chloride ions with respect to the nanoparticle center, and (b) distributions of ligand charges and Chloride ions along the direction of the applied electric field for a C4P32 gold nanoparticle calculated with different electric fields. The unit of electric field is kcal $\cdot$ mol^{-1} $\cdot$ Å^{-1} $\cdot$ e^{-1}.

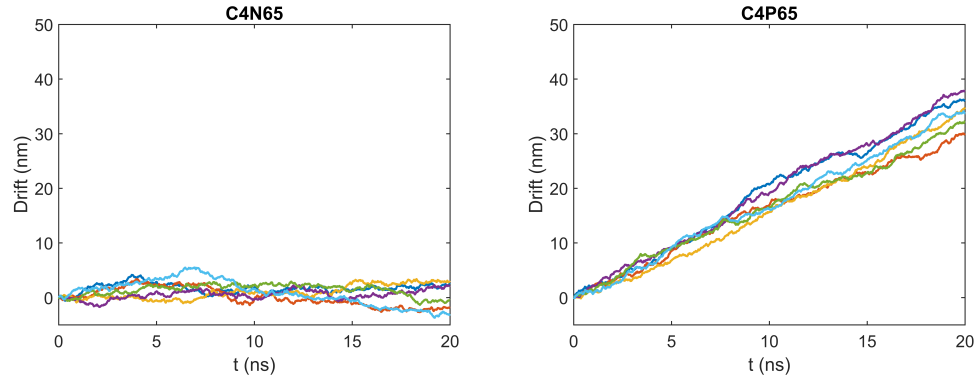

(a) (b)

Figure S10: Drift of C4N65 and C4P65 in 150 mM NaCl during drift velocity simulations. The multiple curves are independent runs where the electric field is applied in $\pm x$, $\pm y$ or $\pm z$ directions. The electric field applied is 0.05 kcal $\cdot$ mol^{-1} $\cdot$ Å^{-1} $\cdot$ e^{-1}. The first 10 ns of each trajectory is excluded from the figure and analysis.

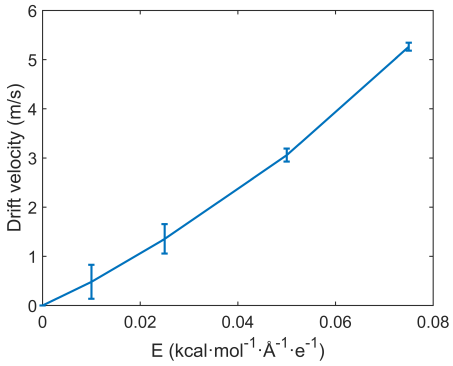

(a)

Figure S11: Drift velocities of a C4P32 gold nanoparticle calculated with different electric fields. Each data point is averaged over 3 independent runs. The results show that $E = 0.05$ provides a favorable compromise between accuracy and efficiency.

Table S2: Mobilities of different nanoparticles from independent drift velocity simulations with electric fields applied in different directions. The unit of mobility is $10^{-4} \cdot \text{cm}^2 \cdot \text{V}^{-1} \cdot \text{s}^{-1}$, the electric field applied is 0.05 kcal $\cdot$ mol^{-1} $\cdot$ Å^{-1} $\cdot$ e^{-1}.

50 mM NaCl						
Nanoparticle	-x	-y	-z	+x	+y	+z
C4Q65	13.68±0.02	13.07±0.01	12.50±0.03	13.21±0.02	12.47±0.02	13.39±0.01
C4P65	10.98±0.02	10.19±0.01	11.71±0.01	11.66±0.02	10.35±0.01	11.25±0.03
150 mM NaCl						
Nanoparticle	-x	-y	-z	+x	+y	+z
C4Q65	9.10±0.02	9.47±0.02	9.10±0.01	9.73±0.01	9.17±0.02	8.63±0.03
C4P65	8.29±0.02	6.52±0.01	7.90±0.01	7.32±0.01	6.58±0.02	8.49±0.01
C8P32-C4P33	7.43±0.03	8.18±0.02	8.62±0.02	9.85±0.02	9.58±0.02	8.23±0.02
C4P32-C4N33	10.47±0.03	7.69±0.02	9.72±0.05	7.97±0.02	9.54±0.03	8.79±0.02
C4P32-C4C33	10.34±0.02	9.76±0.02	10.45±0.02	8.18±0.04	10.69±0.03	9.88±0.01
C4N65	1.16±0.01	-0.76±0.01	-0.95±0.01	-0.45±0.02	-0.12±0.02	0.26±0.02

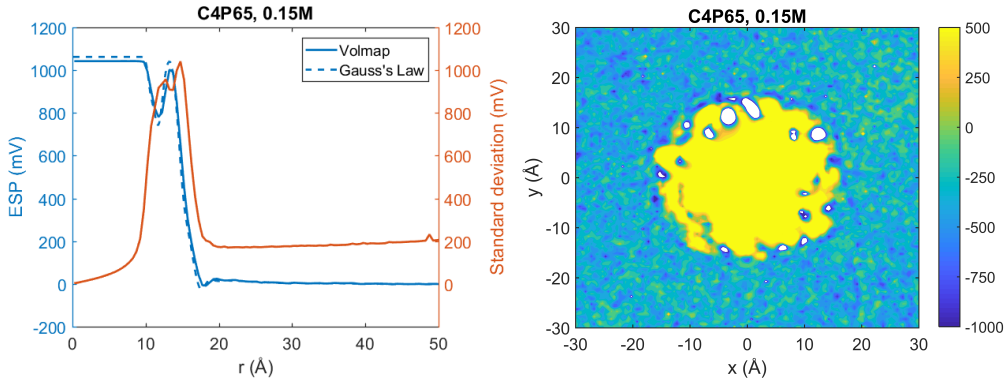

(a) (b)

Figure S12: Electrostatic potential profile calculated with the Volmap tool of VMD averaged over 1000 frames from 10 ns of equilibrium simulation for the C4P65 nanoparticle in 150 mM NaCl solution. (a) Comparison between Volmap averaged result with Gauss's Law result shows excellent consistency. The angular standard deviation of the potential as a function of distance is also shown in red. (b) A two-dimensional slice of electrostatic potential cross the nanoparticle center.

3 Binding Free Energy of a 50% protonated Asp_8 peptide to Nanoparticles

To probe whether the key results discussed in the main text apply to less charged biomolecules, we have conducted umbrella sampling simulations to compute the binding free energy of the same Asp_8 peptide, but with the sidechains adopting alternating protonation states; i.e., 50% of the sidechains are protonated, leading to a net charge of -4 rather than -8. This particular choice is made based on several considerations: (1) we aim to focus on binding driven by electrostatic interactions, thus a mixture of charged and protonated (thus charge neutral) Asp sidechains reflect the combination of charged and polar residues, which are representative of protein surfaces; (2) the relatively homogeneous sequence avoids slow convergence of binding free energy simulations. The simulation protocols are identical to those reported in the main text for the fully ionized Asp_8 peptide.

As shown in Fig. S13, the binding free energy profiles for the 50% ionized Asp_8 resemble those for the fully ionized peptide, especially when the statistical uncertainty of the computed PMFs are considered. Most importantly, the results support the key trend that the strength of binding is dictated by the bare charge density of the nanoparticle.

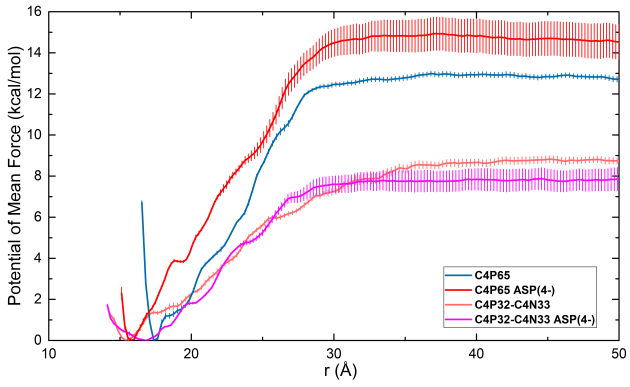

Figure S13: Potential of mean force of a 50% protonated Asp_8 peptide binding to different nanoparticles in 150 mM NaCl solution from umbrella sampling simulations. The r as shown is defined as the distance between the nanoparticle center and the center of mass of the peptide.

4 Additional Simulation for a Different Nanoparticle Model

To probe whether the key properties of the electric double layer are sensitive to the precise model of the functionalized gold nanoparticle, we have simulated a system using the latest nanomaterials module of CHARMM-GUI,[1] which offers several approaches for building nanoparticles (http://www.charmm-gui.org/?doc=input/nanomaterial). In particular, we have selected a core structure that resembles the crystal structure of small gold-thiol clusters: $Au_{279}(SR)_{84}$. (see Fig. S14 for a snapshot), which features the staple motif discussed in several previous studies.[2–4] With this core structure, we have conducted simulations with two functionalization patterns: one with all eighty-four butyl amines protonated (C4P84, in which SR=$SC_4H_8(NH_3)^+$), and one with randomly selected 50% of the butyl amines protonated (C4P42-C4N42, i.e., SR_1=$SC_4H_8(NH_3)^+$ and SR_2=$SC_4H_8(NH_2)$). The simulation protocols are identical to those reported in the main text for other nanoparticle systems, and the salt concentration is 150 mM.

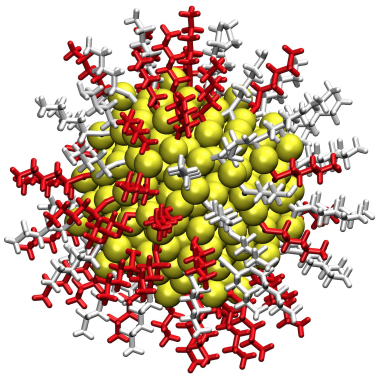

Figure S14: A snapshot of the gold cluster model ($Au_{279}(SR)_{84}$) with a core structure that features the staple motif discussed in previous work. The snapshot illustrates the functionalization pattern in which 50% of the butyl amines are deprotonated (white) while the rest protonated (red).

In Fig. S15, we summarize the key properties of the functionalized gold cluster model, including radial distribution of Cl^- ions, the radial apparent charge profile (Q_{app}), and the

interfacial electrostatic potential profiles. Compared to the spherical nanoparticle models discussed in the main text, the results for the gold cluster models exhibit the same key trends. In particular, at 150 mM, the compensation due to the counter ions is almost at the level of saturation so that the apparent charges (panel b) and interfacial electrostatic potentials (panel d) are practically identical for the two gold clusters of different bare charges. The interfacial potential reaches a fairly constant value of <10 mV for both cluster models, comparable to those observed for the spherical nanoparticle models (Table 4 in the main text and Fig. S4b). Therefore, we conclude that the key trends discussed in the main text are not sensitive to the model of the nanoparticle core structure.

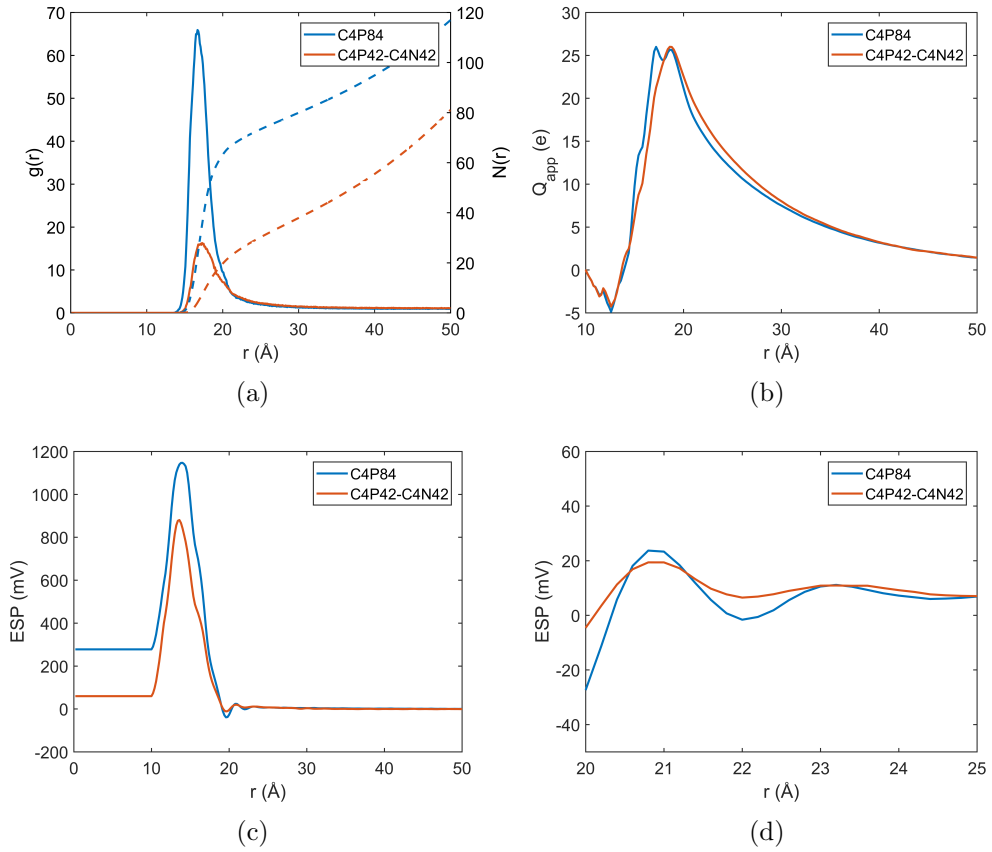

Figure S15: Properties of the electric double layer for the functionalized gold cluster models. (a) Radial distribution function of chloride ions with respect to the cluster center; the dashed lines are integrated radial distribution functions. (b) Computed apparent charge ($Q_{app}(r)$) profile as a function of distance from the cluster center; $Q_{app}(r)$ includes bare ligand charges and counterion charges up to distance r. (c-d) Computed electrostatic potential (ESP) as a function of distance from the cluster center; panel c shows the overall profile, while panel d enlarges the interfacial region.

5 Experimental Measurements of ζ-potentials

We measured ζ potential for three nanodiamond particles (5 nm in diameter) functionalized with primary amines (C3P), quaternary amines (C3Q) and a 1:1 mixture of quaternary amines and methyl ether (C3Q-C3M); these were inspired by the C4P, C4Q and C4Q-C4M particles studied computationally in the main text. Nanodiamonds instead of gold nanoparticles were used because it was more straightforward to functionalize nanodiamonds, especially with a mixture of different ligands, using the radical-based method introduced recently by two of us.[5] The measurements were done at three NaCl concentrations: 0 mM, 10 mM and 50 mM. As shown in Table S3, the three particles are substantially larger in size compared to the gold nanoparticles studied computationally and the original nanodiamond prior to functionalization, indicating a considerable degree of aggregation especially at higher salt concentrations. Therefore, the comparison with the computational results should be taken with care. Nevertheless, we observe that counterions significantly impact the measured ζ potential even at the moderate salt concentration of 50 mM. Moreover, the impact is largest for the primary amine functionalized particle, whose ζ potential drops from +46 $\pm$1.4 mV at 0 mM NaCl to +17$\pm$1.0 mV at 50 mM NaCl; by comparison, the quaternary amine functionalized nanoparticle has a similar ζ potential at 0 mM NaCl (+44$\pm$1.6 mV) but a *higher* ζ potential at 10 and 50 mM NaCl. These trends are qualitatively consistent with the computational results discussed in the main text, supporting the importance of counterion association and its dependence on the chemical nature of the charged ligand. By mixing in the methyl ether ligands, which feature a hydrophobic terminal group (-OCH_3), the salt dependence of ζ potential is further reduced, especially at 50 mM. While this result should be interpreted with care as the C3Q-C3M particles appear to be larger in size, suggesting a higher degree of aggregation, the observation supports the general conclusion of the computational result that introducing hydrophobic surface groups modulates the interfacial electrostatic properties.

Preparation of different amine functionalized diamond nanoparticles

Detonation nanodiamond (5 nm average primary particle diameter, Nanstructured & Amorphous Material Inc.) was used, and DNPs were functionalized with propylamine (C3P), propyl-trimethylammonium (C3Q) using a radical-based method that has described in Zhang et al.[5] The methyl ether/amine mixed surfaces were functionalized using a 1:1 mixture of propyl trimethylammonium and propyl methyl ether (C3Q-C3M). The ligand density is approximately 0.7 ligand/nm^2, as measured in previous work.[5]

Mobility and ζ potential measurements of amine-functionalized DNPs

The mobility, ζ potential and the hydrodynamic diameter of the sample were measured at 298 K with a scattering angle of 173° (Malvern Zetasizer NanoZS). The values reported here were obtained from five separate measurements, each with ten sub-runs. All mobility and ζ potential measurements were done using the Malvern universal dip cell with palladium electrodes. The hydrodynamic diameter measurements were done using the 10 mm path length 3.5 mL plastic Malvern cuvette.

Table S3: Experimentally measured hydrodynamic diameter (in nm), ζ potential (in mV) and mobility μ (in 10^{-4}cm^2/(V·s)) for three types of functionalized nanodiamond particles in water solutions of different NaCl concentrations.

Particle	Diameter (nm)			ζ (mV)			μ (10^{-4}cm^2/(V·s))		
	0 mM	10 mM	50 mM	0 mM	10 mM	50 mM	0 mM	10 mM	50 mM
C3P	22.8±0.9	27.0±0.7	–	46±1.4	30±0.3	17±1.0	3.6±0.1	2.3±0.0	1.4±0.1
C3Q	28.9±0.7	30.7±0.6	–	44±1.6	40±1.5	24±3.5	3.4±0.1	3.2±0.1	1.9±0.3
C3Q-C3M	48.0±0.8	63.9±4.5	–	41±1.5	31±0.6	30±0.8	3.2±0.1	2.5±0.1	2.4±0.1

References

(1) Jo, S.; Kim, T.; Iyer, V. G.; Im, W. CHARMM-GUI: a web-based graphical user interface for CHARMM. *J. Comput. Chem.* **2008**, *29*, 1859–1865.

(2) Sakthivel, N. A.; Theivendran, S.; Ganeshraj, V.; Oliver, A. G.; Dass, A. Crystal Structure of Faradaurate-279: Au_{279}(SPh-tBu)$_{84}$ Plasmonic Nanocrystal Molecules. *J. Am. Chem. Soc.* **2017**, *139*, 15450–15459.

(3) Heikkila, E.; Martinez-Seara, H.; Gurtovenko, A. A.; Vattulainen, I.; Akola, J. Atomistic simulations of anionic Au-144(SR)(60) nanoparticles interacting with asymmetric model lipid membranes. *Biochim. Biophys. Acta-Biomembranes* **2014**, *1838*, 2852–2860.

(4) Heikkilä, E.; Gurtovenko, A. A.; Martinez-Seara, H.; Häkkinen, H.; Vattulainen, I.; Akola, J. Atomistic Simulations of Functional $Au_{144}(SR)_{60}$ Gold Nanoparticles in Aqueous Environment. *J. Phys. Chem. C* **2012**, *116*, 9805–9815.

(5) Zhang, Y. Q.; Tamijani, A. A.; Taylor, M. E.; Zhi, B.; Haynes, C. L.; Mason, S. E.; Hamers, R. J. Molecular surface functionalization of carbon materials via radical-induced grafting of terminal alkenes. *J. Am. Chem. Soc.* **2019**, *141*, 8277–8288.